Dynamic Analysis and Numerical Modeling of the 2015 Catastrophic Landslide of the Construction Waste Landfill at Guangming, Shenzhen, China

Chaojun Ouyang[1,*], Kaiqi Zhou[2], Qiang Xu[3], Jianhua Yin[4], Dalei Peng[3], Dongpo Wang[3], Weile Li[3]

[1)] *Key laboratory of Mountain Hazards and Surface Process & Institute of Mountain Hazards and Environment (IMHE), Chinese Academy of Sciences, Chengdu, 610041, China*

[2)]*Department of Mechanics, Huazhong University of Science and Technology, Wuhan, 430074, China*

[3)]*National Laboratory of Geohazard Prevention and Geoenvironment Protection, Chengdu University of Technology, Chengdu 610059, China*

[4)]*Department of Civil and Environmental Engineering, The Hong Kong Polytechnic University, Hong Kong, China*

The corresponding author email: cjouyang@imde.ac.cn

Abstract: Since lots of underground and slope excavation works were conducted during the urbanization process, an increasing number of sites in ravines around a city have been used to stockpile of a large amount of excavated soils. This brings a huge challenge for researchers and managers in the risk evaluation and mitigation of potential dangers of these man-made construction waste landfills. This paper describes a recently large landslide of the construction waste landfill, which occurred at a site of Guangming new district in Shenzhen, China on December 20, 2015. This catastrophic landslide caused the death of 69 persons and 8 persons stilling missing. In this paper, this landslide was numerically simulated and analyzed. In spite of neither high intensity rainfall and nor antecedent rainfall, a slope of this landfill with a relative height of 111 m sided and caused about 2.34 million cubic meters of the soils

traveled over a gentle terrain more than 1.2 km. This means that landslide mobility index (H/L = 0.092) is much lower than a general designed value and the values in most other cases. A depth-integrated continuum method and a MacCormack-TVD finite difference algorithm are adopted, in this paper, to numerically simulate the dynamic process of this large landslide. It is found that that a Coulomb friction model with consideration of the pore water pressure effects can well reproduce the main characteristics of the dynamic process of this landslide. Sensitivity analysis has demonstrated that the high pore water pressure in the soils plays a significant role in its mobility and is a key factor to the severity of this landslide.

Keywords: Landslide; Excess pore water pressure; Mobility; MacCormack-TVD scheme; Numerical modeling; Landfill

1 Introduction

The site selection and its safety of waste soil landfill is a prominent problem due to project construction or developing urbanization. On December 20, 2015, a catastrophic landslide of the construction waste landfill suddenly collapsed and rushed down to the residential buildings and industrial zones at Guangming, Shenzhen, China (E113°56'5", N22°42'44"). It destroyed 33 buildings and caused 69 deaths and 8 losses, which was one of the most devastating accidents (Yin et al., 2016). Of concern is that mounts of similar man-made landfills exist widely (Jafari et al., 2013; Lavigne et al., 2014). Landslide risk evaluation and hazard reduction are a huge challenge for researchers and engineers to prevent disastrous causes (Cruden and Varnes, 1996; Van Westen et al., 2006; Yin et al., 2009). Reliably determining when or where every landslide would happen ahead of time in a vast area is still too difficult due to its complexity (Kirschbaum et al., 2015). Nevertheless, it is significantly important to perform reliable risk evaluation and hazardous area prediction for the identified landslides which are judged as potential possibility of failure (Dai et al., 2002; Van Westen et al., 2006).

The damage to structures and properties from landslide mainly refers to debris deposition and its huge impact force (Huang et al., 2007; Wang et al., 2008). Prevention of losses requires to know the maximum travel distance and deposition area of landslide. It has been long realized that the landslide mobility index, defined as H/L (ratio of height to distance), can be utilized to generally evaluate its runout characteristics (Corominas, 1996; Iverson et al., 2015). Commonly, H/L<0.3 is deemed as high mobility even for soil with low internal friction angle and at this condition it could travel three times further than its relative height. However, an increasing number of catastrophic events indicate that H/L could even reduce to about 0.1 for classical rock-soil mass (Legros, 2002; Hunter and Fell, 2003; Iverson et al., 2015). Large range of landslide mobility (0.1~3) brings a big challenge in site selection, risk analysis and mitigation (Dai et al., 2002).

Numerical modeling provides a feasible method for dynamic process and risk evaluation of landslide. A mount of quantitative numerical methods including discrete element method (Tang et al., 2009; Lo et al., 2014), smoothed particle hydrodynamics (Pastor et al., 2009; Huang et al., 2012), depth-integrated continuum mechanics method (Pirulli, 2005; Wang and Sassa, 2010) or other numerical techniques (Chung and Fabbri, 1999; Quecedo, et al., 2004; Ataie-Ashthiani and Yavari-Ramshe, 2011) have been demonstrated their capacity of reproducing dynamic process of landslide. More and more two- and three-dimensional discrete element method is adopted to analyze landslide process and good results are obtained if particle parameters were calibrated (Zhao et al., 2006; Banton et al., 2009). The mesh-free smoothed particle hydrodynamics method has also been applied in modeling in landslide over natural terrain (Liu and Liu, 2003). Discrete element method and smoothed particle hydrodynamics have specific advantages in modelling complex three–dimensional environmental fluid and particulate flows, whereas they are still severely constrained by their time-consuming computation (Cleary and Prakash, 2004). Depth-integrated continuum model was firstly suggested by Savage and Hutter (1989) and has been successfully applied in extensive earth-surfaced flows such as landslide (McDougall and Hungr, 2004), debris flow (George and Iverson, 2011; Ouyang et al., 2015a),

hydrodynamic (Liang, 2010; Ouyang et al., 2015b), rock or snow avalanche (Delaney and Evans, 2015) and so on. Based on depth-integrated continuum model, several physical mechanism and model were suggested to describe the high mobility of landslide. The depth-integrated continuum model considering excess pore water pressure generation and dissipation due to soil deformation was adopted to investigate the liquefaction and high mobility mechanism of 2014 Oso landslide, Washington, USA (Iverson and George, 2015). In addition, the thermo-poro-elastic mechanism, which coupled the frictional heating and excess pore pressure generation in sliding plane, was deemed to be another mechanism of the high mobility of huge landslide (He, et al., 2015). However the above-mentioned pore water pressure evolution treatment involved in complicated mechanism and much more parameters, it remains further enhanced.

In this paper, the landslide at Guangming new district on December 20, 2015 in Shenzhen, China is analyzed in detail. Firstly, the geological conditions, causes and mechanisms of the landslide are introduced. Secondly, the depth-integrated continuum framework and Coulomb friction model with consideration of pore water pressure effect are described. MacCormack-TVD finite difference algorithm which owns second-order accuracy in both time and space is introduced (Liang et al., 2006; Ouyang et al., 2013). Thirdly, the numerical analysis compared with field investigation and parameter sensitivity of pore water pressure coefficient are performed. In the end, some implication and conclusion are discussed.

2 Backgrounds

2.1 Geological conditions and soil properties

The landslide site is located at a new development district of Guangming region, 23 km northwest of center of Shenzhen, Guangdong, China (E113°56'5", N22°42'44"). From the view of Google map, the location was previously a stone pit since 2005 and formed an area of 2.66×10^4 m^2 big hollow filled with water in 2013. Since 2014, the pit started to dump in loose excavated soil without excluding the bottom water. In less

than two years, a total volume of 6.27×10^4 m^3 was quickly filled in and almost ten terraces at a ratio of 1:2.5 were formed, as shown in Fig. 1(a).

The bedrock of the dumpsite is mainly Cretaceous granite rock. The landfill derives from a wealth of sources and mainly consists of construction waste with silty soil, clay, rock and gravel. The soil for laboratory experiments were sampled from four different locations, as marked by #1-#4 in Fig. 1(b). The engineering geological map and engineering geological profile are provided in Figs. (2) and (3). Grain size analysis was conducted by using the wet sieve method and the particle size distribution curves are shown in Fig. 4. The mineral composition of waste fill and bedrock are listed in Table 1. Based on in-situ waste filling density and moisture content tests as well as the laboratory compaction test, it was found that the dry density varies from 1.25 to 1.48 g/cm3 and void ratio ranged between 0.83 and 1.31. The volume expansion coefficient of the landslide was 1.007. Standard compaction test demonstrated that the optimal water content of the waste filling was 15.31% with the highest dry density of 1.79 g/cm^3. Triaxial undrained shear test estimated that cohesion and internal friction angle of the waste filling is 4.7 kPa and 31.9°, respectively.

2.2 Causes and Failure mechanisms

The average annual rainfall in Shenzhen is about 1966 mm and 85% rainfall is experienced between April to September (Zhang et al., 2006). Based on the precipitation records from the nearby Tangjia rainfall station between Jan 1, 2013 and Dec 20, 2015, the accumulated precipitation in the study area was nearly 3240 mm, as shown in Fig. 5. The catchment area is 4.7×10^5 m^2 which is about three times of source area of 1.6×10^5 m^2. As the drainage system is almost out of work, amounts of water flows into the body of loose soil. The Fig 6 of the deposition zone clearly demonstrates that the soil is almost fully liquefied in the sliding surface due to plenty of water. Thus, it is highly possible that plenty of water was stored in the waste fill.

However, limit equilibrium analysis demonstrated that, even for saturated waste fill, it was still insufficient to induce whole collapse (Xu et al., 2016). Thus， the high

excess pore water pressure could be generated and it actually played a significant role in the landslide failure and the movement. Generation of high excess pore water pressure in this event could be originated from the following two factors. In one hands, as the dumpsite was contained with plenty of water, excess pore water pressure could be generated due to the compaction process with the rapid loading of waste. In the other hands, the witnesses introduced that there was a persistent creep deformation in the front land for 5 hours. As the void ratio is large in the loosely fill, the creep deformation would cause the sand contraction and excess pore water pressure. In addition, the relative height of the landslide was 111 m, whereas it traveled more than 1.2 km. The landslide mobility index H/L is even smaller than 0.1, which is very uncommon and meaningful. The unexpected long-distance traveling is a crucial factor for its catastrophic consequence and deep investigation is worthy.

2.3 Reconstruction of geometry and topography

It is very significant for numerical modeling to obtain the terrain data before and after landslide. As the convenience of unmanned aerial vehicle (UAV)，reconstruction of the terrain from images from the UAV is popular with scientists. In order to improve the resolution from aerial images, it is essential to calibrate the data from GPS station or other ground-based devices. For the Shenzhen landslide, a Pleiades remote sensing image of the study area obtained on Dec 18, 2015 (2 days before the event) was used to create terrain data of before landslide, as shown in Fig. 1(a). Aerial photos with resolution of 5 cm were collected by UAV in 3 days after the landslide, as shown in Fig. 1(b). Ground-based GPS stations were located at four undisturbed and identifiable sites which surrounded the moved waste soil at four different corners. The procedure of reconstruction of the DEM data needs to be calibrated by the geographic information at GPS station. Thus, a high-resolution of terrain data is reconstructed by the images and the information from the GPS station.

3 Model descriptions

3.1 Governing equations of depth-integrated continuum model

Considering the large-scale time and space evolution of geohazards, the

complicated three-dimensional Navier-Stokes equations are generally integrated in vertical direction and reduced into two-dimensional time-consuming problem by neglecting the tiny terms. By strictly deriving from multi-layer flow model, a generalized depth-integrated mass and momentum conservation equations are reformulated as following (Iverson and Ouyang, 2015),

$$\frac{\partial(\bar{\rho}h)}{\partial t}+\frac{\partial(\bar{\rho}h\bar{u})}{\partial x}+\frac{\partial(\bar{\rho}h\bar{v})}{\partial y}-\bar{\rho}\xi E=0 \quad (1)$$

$$\frac{\partial(\bar{\rho}h\bar{u})}{\partial t}+\frac{\partial(\beta_{uu}\bar{\rho}h\bar{u}^2)}{\partial x}+\frac{\partial(\beta_{uv}\bar{\rho}h\bar{u}\,\bar{v})}{\partial y}=\bar{\rho}g_x h-k_{ap}\bar{\rho}g_z h\frac{\partial(h+z_b)}{\partial x}-(\tau_{zx})_b+\bar{\rho}\xi u_b E \quad (2)$$

$$\frac{\partial(\bar{\rho}h\bar{v})}{\partial t}+\frac{\partial(\beta_{uv}\bar{\rho}h\bar{u}\,\bar{v})}{\partial x}+\frac{\partial(\beta_{vv}\bar{\rho}h\bar{v}^2)}{\partial y}=\bar{\rho}g_y h-k_{ap}\bar{\rho}g_z h\frac{\partial(h+z_b)}{\partial y}-(\tau_{zy})_b+\bar{\rho}\xi v_b E \quad (3)$$

where $\bar{\rho}$ represents flow density; h is flow height. u_1 and v_1 are depth-integrated flow velocity in x and y direction; $(\tau_{zx})_b$ and $(\tau_{zy})_b$ are basal resistance components; E is basal entrainment rate; (g_x, g_y, g_z) represent the gravity component on coordinate axis. β is momentum distribution coefficient; k_{ap} is lateral earth pressure coefficient; $\xi=\sqrt{1+(\partial z_b/\partial x)^2+(\partial z_b/\partial y)^2}$ can be integrated as geometric correction coefficient.

For the 2015 Guangming landslide, the soil density between the initial and deposition zone did not expand apparently as the soil was loosely dumped. The volume expansion coefficient of flowslide was 1.007. Thus, $\bar{\rho}$ can be considered to be constant and it can be eliminated on the left sides of the equations. In addition, in spite of the breach zone, it is found that the basal soil erosion in the downstream zone is limited, so the terms associated with entrainment could be neglected. If the effects from momentum distribution coefficient β are neglected (e.g. β =1), the mass and momentum equations (1)-(3) in rectangular Cartesian with vertical z-axis reduce to

$$\frac{\partial(h)}{\partial t}+\frac{\partial(h\bar{u})}{\partial x}+\frac{\partial(h\bar{v})}{\partial y}=0 \quad (4)$$

$$\frac{\partial(h\bar{u})}{\partial t}+\frac{\partial(h\bar{u}^2+k_{ap}gh^2/2)}{\partial x}+\frac{\partial(h\bar{u}\,\bar{v})}{\partial y}=k_{ap}gh\frac{\partial z_b}{\partial x}-\frac{(\tau_{zx})_b}{\bar{\rho}} \quad (5)$$

$$\frac{\partial(h\bar{v})}{\partial t}+\frac{\partial(h\bar{u}\,\bar{v})}{\partial x}+\frac{\partial(h\bar{v}^2+k_{ap}gh^2/2)}{\partial y}=k_{ap}gh\frac{\partial z_b}{\partial y}-\frac{(\tau_{zy})_b}{\bar{\rho}} \quad (6)$$

where k_{ap} is lateral earth pressure coefficient. Its value depends on the strain rate of the moving material columns and appears active status on elongation and passive status on compression. The expression suggested by Savage and Hutter (1989) is as follows

$$k_{ap}=\frac{2}{\cos^2\phi}\times\left[1\mp\sqrt{1-(1+\tan^2\delta)\cos^2\phi}\right]-1 \quad (7)$$

where ϕ and δ are the internal and basal friction angles of the flow material. k_{ap} is active status for diverging flow (indicated by $\frac{\partial\bar{u}}{\partial x}+\frac{\partial\bar{v}}{\partial x}>0$) and positive status for converging flow (indicated by $\frac{\partial\bar{u}}{\partial x}+\frac{\partial\bar{v}}{\partial x}<0$).

τ_b is assumed to obey Coulomb failure criterion as follows

$$\tau_b=c+\bar{\rho}gh(1-\lambda)\tan(\phi) \quad (8)$$

c and ϕ are cohesion and friction angle of the mass; λ is a pore pressure ratio that indicates the degree of liquefaction of the bed material. Its value ranges from 0 (ex. dry avalanche) to 1 (ex. completely saturated debris). The pore water pressure generation and dissipation are influenced by granular dilatancy and hydraulic diffusivity. Pore water pressure evolutional process is complicated and a uniform λ is currently considered for simplification.

3.2 Numerical implementation

The conservation equations (4)-(6) are solved by finite difference method based on a MacCormack-TVD scheme (Liang et al., 2006; Ouyang et al., 2013). The

computational process is implemented by using Fortran programming. Firstly, the equations (4)-(6) are expressed in vector format

$$\frac{\partial \mathbf{X}}{\partial t}+\frac{\partial \mathbf{F}}{\partial x}+\frac{\partial \mathbf{G}}{\partial y}=\mathbf{S}+\mathbf{T} \quad , \tag{9}$$

in which

$$\mathbf{X}=\begin{Bmatrix} h \\ h\bar{u} \\ h\bar{v} \end{Bmatrix} \quad ; \qquad \mathbf{F}=\begin{Bmatrix} h\bar{u} \\ h\bar{u}\,\bar{u}+\dfrac{k_{ap}gh^2}{2} \\ h\bar{u}\,\bar{v} \end{Bmatrix} \quad ; \qquad \mathbf{G}=\begin{Bmatrix} h\bar{v} \\ h\bar{u}\,\bar{v} \\ h\bar{v}\,\bar{v}+\dfrac{k_{ap}gh^2}{2} \end{Bmatrix}; \tag{10}$$

$$\mathbf{S}=\begin{Bmatrix} 0 \\ k_{ap}gh\dfrac{\partial z_b}{\partial x}-gh(1-\lambda)\tan(\phi)\bar{u}/\sqrt{\bar{u}^2+\bar{v}^2} \\ 0 \end{Bmatrix}; \mathbf{T}=\begin{Bmatrix} 0 \\ 0 \\ k_{ap}gh\dfrac{\partial z_b}{\partial y}-gh(1-\lambda)\tan(\phi)\bar{v}/\sqrt{\bar{u}^2+\bar{v}^2} \end{Bmatrix}$$

Then the vectorized equation (9) is divided into two separate one-dimensional problems by the operator-splitting technique as follows

$$\frac{\partial \mathbf{X}}{\partial t}+\frac{\partial \mathbf{F}}{\partial x}=\mathbf{S}\,; \qquad \frac{\partial \mathbf{X}}{\partial t}+\frac{\partial \mathbf{G}}{\partial y}=\mathbf{T} \tag{11a, b}$$

The updated quantities at next step are computed by the Strang type operator splitting

$$\mathbf{X}_{i,j}^{n+1}=L_x2(\frac{\Delta t}{2})L_y2(\frac{\Delta t}{2})L_y1(\frac{\Delta t}{2})L_x1(\frac{\Delta t}{2})\mathbf{X}_{i,j}^{n} \quad , \tag{12}$$

where L_x and L_y represent a predictor-corrector-averaged computational procedure. Each splitting operator is treated twice to gain the solution at the next step.

For each splitting operator, taking L_x1 for example, its computation can be given by

$$\mathbf{X}_{i,j}^{p}=\mathbf{X}_{i,j}^{n}-(\mathbf{F}_{i,j}^{n}-\mathbf{F}_{i-1,j}^{n})\cdot\frac{\Delta t}{2\Delta x}+\mathbf{S}_{i,j}^{n}\cdot\Delta t/2 \quad , \tag{13}$$

$$\mathbf{X}_{i,j}^{c} = \mathbf{X}_{i,j}^{n} - (\mathbf{F}_{i+1,j}^{p} - \mathbf{F}_{i,j}^{p}) \cdot \frac{\Delta t}{2\Delta x} + \mathbf{S}_{i,j}^{p} \cdot \Delta t / 2 \quad , \tag{14}$$

$$\begin{aligned} \mathbf{X}_{i,j}^{n+1/2} = (\mathbf{X}_{i,j}^{p} + \mathbf{X}_{i,j}^{c})/2 + [G(\mathbf{r}_{i,j}^{+}) + G(\mathbf{r}_{i+1,j}^{-})]\Delta\mathbf{X}_{i+1/2,j}^{n} \\ - [G(\mathbf{r}_{i-1,j}^{+}) + G(\mathbf{r}_{i,j}^{-})]\Delta\mathbf{X}_{i-1/2,j}^{n} \end{aligned} \quad , \tag{15}$$

where the superscripts p and c mean the predictor and corrector steps. The second and third terms on the right of equation (15) are adopted to gain second-order precision and avoid numerical oscillation. $\mathbf{r}^{+-}$ is a scalar function relative to five neighboring nodes. It is expressed as

$$\mathbf{r}_{i,j}^{+} = \frac{(\Delta\mathbf{X}_{i-1/2,j}^{n}, \Delta\mathbf{X}_{i+1/2,j}^{n})}{(\Delta\mathbf{X}_{i+1/2,j}^{n}, \Delta\mathbf{X}_{i+1/2,j}^{n})}; \qquad \mathbf{r}_{i,j}^{-} = \frac{(\Delta\mathbf{X}_{i-1/2,j}^{n}, \Delta\mathbf{X}_{i+1/2,j}^{n})}{(\Delta\mathbf{X}_{i-1/2,j}^{n}, \Delta\mathbf{X}_{i-1/2,j}^{n})} \tag{16}$$

where

$$\Delta\mathbf{X}_{i+1/2,j}^{n} = (\mathbf{X}_{i+1,j}^{n} - \mathbf{X}_{i,j}^{n}); \qquad \Delta\mathbf{X}_{i-1/2,j}^{n} = (\mathbf{X}_{i,j}^{n} - \mathbf{X}_{i-1,j}^{n}) \quad . \tag{17}$$

The function $G()$ is expressed as

$$G(\theta) = 0.5 \times C \times [2 - \varphi(\theta)] \quad , \tag{18}$$

in which function $\varphi(\theta)$ is a flux limiter function. Here the MC limiter (Van Leer, 1979) is adopted and it is written as

$$\varphi(\theta) = \max(0, \min(2, 2\theta, \frac{1+\theta}{2}) \quad , \tag{19}$$

where θ is a function variable. The variable C is expressed as

$$C = \begin{cases} Cr \times (1 - Cr) & \mathrm{Cr} \le 0.5 \\ 0.25 & \mathrm{Cr} > 0.5 \end{cases} \quad , \tag{20}$$

where Cr is the local Courant number, which is used to constrain the time step and defined as

$$Cr = \frac{(|\bar{u}| + \sqrt{gh})\Delta t}{2\Delta x} \quad . \tag{21}$$

The time step is constrained by the Courant formula as

$$\Delta t = \min\left(\frac{2\Delta xCr}{(|\bar{u}| + \sqrt{gh})}, \frac{2\Delta yCr}{(|\bar{v}| + \sqrt{gh})}\right). \quad (22)$$

4 Numerical analysis of the 2015 catastrophic landslide in Guangming new district of Shenzhen, China

4.1 Determination of the topography and the initial source of landslide

In order to determine the area and volume of initial source, the terrain data before and after landslide is both needed. The pre-event topography is obtained from aerial images on December 18, 2015 and calibrated by total station. The post-event topography is generated from low-altitude photogrammetry and ground-based GPS station. As suggested by Iverson and George (2015), the reconstruction of the sliding surface is needed as considerable material remains in the source zone. Nevertheless, for the abandoned soil, it is difficult to recognize the tail boundary of moving material. Thus, we take the topography difference before and after landslide adding the measured average deposition depth as the initial source. The average deposition depth is estimated to be about 8.21 m (Xu et al., 2016). The total initial volume in the computation is 3.27×10^6 m^3. In fact, the addition of the average deposition depth or not won't change the whole runout behavior a lot, which mainly influences the deposition behavior in the source zone. In the computation, a uniform high-resolution of 2 m grid was adopted.

4.2 Computational model and parameters

The basal friction model plays a key role in landslide's dynamic characteristics.

Here, Coulomb friction model with consideration of effect of pore water pressure is chosen as it is simple and the parameters are physical-based. In order to provide a reliable referred method for risk evaluation of such kind of abandoned soil landslide, we prefer to use parameters as less as possible. The Coulomb friction model in equation (8) needs three parameters including cohesion, internal friction angle and pore water pressure coefficient. In the fast sliding process, effect from the cohesion in the sliding base can be neglected. The measured internal friction angle by triaxial experiment is about 31.9°. The high pore water pressure generation or dissipation in the sliding base is complicated as it referred to its dynamic evolution involved several factors (Wang and Sassa, 2003; Iverson et al., 2015). Nevertheless, it is convenient and feasible to use a constant pore water pressure coefficient for simplification. Guangming landslide is a man-made disaster due to disabled drain system (Xu et al., 2016). Multiple evidences demonstrated that the enriched water and high pore water pressure played a determining role in its super mobility. Back analysis shows that λ value of 0.75 agrees well with the investigated results. The sensitivity of pore water pressure coefficient is also analyzed and it is demonstrated that high pore water pressure is a significant factor to cause its long-distance runout. The computational cell size is set as 2 m and the variable time step based on Courant rule is chosen for all the cases.

4.3 Analysis of computational results

The internal friction angle is set to be the measured value of 31.9°. Firstly, the

results from pore water pressure coefficient λ=0.75 are analyzed. The density of abandoned soil before and after collapse is nearly same, so the density of moving mass is considered to be constant. In addition, in spite of the breach location, the erosion in the flow zone can be ignored compared with total mass volume. Thus, the effect of entrainment is not taken into account.

The final deposited depth and area in numerical simulation are compared with real deposited data from aerial image and field measurement. The contours of moving flow depth of Guangming landslide at times t=0, 25, 50, 100, 150, 200 seconds are shown in Fig. 7. In addition, a video of landslide dynamic process is provided as supplementary material. Contour from grids with depth lower than 2 meter is eliminated. The maximum depth in the initial source area is 50.5 m. It is shown that the abandoned soil flushed down quickly after it collapses. Then the continuous moving mass in the tank pushed the mass moving in the downstream and lateral direction. After 50 s, the abandoned soil impacted against the arrayed high buildings and it almost stopped after 200 s. The computational volume of deposited mass in the downstream is about 2.60×10^6 m^3 compared to the estimated volume of 2.13×10^6 m^3. It is shown that the main computational flow domain is located in the measured range enclosed by red line. Main deviation is from some soil with lower depth extending in the left region and burying some undamaged buildings, which is unmatched with real situation, is due to the continuum characteristic of depth-integrated model and lack of topography in detail. The comparisons of final surface between simulation and measurement in the main profile A-A and two transverse profiles B-B and C-C are

exhibited in Fig. 8. The schematic profiles are presented in Figs. 1 and 2. In the source zone, ranging from 0 to 500 m in Fig 8(a), the computational profile is generally matched with the deposited surface except in the sharp slope. In the remaining deposition zone, the modeling flow is a little higher near the breach and relatively lower near the border. Nevertheless, the computational influenced area is well satisfied to be assisted in risk evaluation and site selection of building.

The contours of flow velocity of the landslide at times t=25, 50, 100, 150, 200 seconds are shown in Fig. 9. Before the flow impacting the arrayed building, the mass moved at speed excess 20m/s mainly with depth higher than 10 m. The velocity histories over time in four different locations of the main profile are shown in Fig. 10. The locations are marked by S1-S4 in Fig 1(a). It shows that the maximum of velocity is about 39 m/s. It is large enough to destroy all the simple houses and structures. After 150 s, the flow velocity in most part of body is very slow except near the breach due to the steep terrain.

In addition, the influence of different pore water pressure coefficient is investigated. The contours of final deposited depth at 200 s for $\lambda=0, 0.3, 0.6, 0.85$ are shown in Fig. 11. It is demonstrated that the abandoned soil can only move about 100 m if pore water pressure effect is missing ($\lambda=0$). Even for $\lambda=0.6$, the travel distance and influenced area are far less than the measured ones. Whereas $\lambda=0.85$ is chosen, the masses bury most of buildings. Thus, in order to avoid potential hazard risk, a high pore water pressure coefficient needs to be considered.

5 Conclusions

The catastrophic landslide occurred in Guangming new district of Shenzhen, China on December 20，2015 has been simulated and analyzed. The results from the simulation are compared with aerial images and field investigation data. It is demonstrated that the depth-integrated continuum mechanic method with Coulomb friction model coupled with pore water pressure effects is able to well capture the characteristics of the landslide. The internal friction angle can be obtained by experiments and only pore water pressure coefficient needs to be calibrated. The results from the simulation and analysis demonstrate that the constant pore water pressure coefficient can generally reproduce the dynamic process of the landslide. The parameter sensitivity analysis illustrates that the excess pore water pressure is a key factor causing the high mobility and catastrophic impact of this landslide.

Acknowledgments: Financial support from NSFC (Grant No. 41572303, 4151001059), CAS "Light of West China" and Youth Innovation Promotion Association, is acknowledged. The work in this paper is supported by a National State Key Project “973” grant (Grant No. 2014CB047001) from Ministry of Science and Technology of the People’s Republic of China.

References

Ataie-Ashtiani, B., Yavari-Ramshe, S. (2011). Numerical simulation of wave generated by landslide incidents in dam reservoirs. Landslides, 8(4), 417-432.

Banton, J., Villard, P., Jongmans, D., Scavia, C. (2009) Two-dimensional discrete element models of debris avalanches: Parameterization and the reproducibility of experimental results. Journal of Geophysical Research: Earth Surface, 114(F4).

Chung, C., Fabbri, A. G. (1999) Probabilistic prediction models for landslide hazard mapping.

Photogrammetric Engineering and Remote Sensing, 65(12): 1389-1399.

Cleary, P. W., Prakash, M. (2004) Discrete-element modelling and smoothed particle hydrodynamics: potential in the environmental sciences. Philosophical Transactions-royal Society of London Series a -Mathematical Physical and Engineering Sciences, 362: 2003-2030.

Corominas J. The angle of reach as a mobility index for small and large landslides . Canadian Geotechnical Journal, 1996, 33(2): 260-271.

Cruden, D., Varnes, D. (1996) Landslides: investigation and mitigation. Chapter 3-Landslide types and processes. Transportation Research Board Special Report, (247).

Dai, F., Lee, C., Ngai, Y. Y. (2002) Landslide risk assessment and management: an overview. Engineering Geology, 64(1):65-87.

Delaney, K. B., Evans, S. G. (2015) The 2000 Yigong landslide (Tibetan Plateau), rockslide-dammed lake and outburst flood: Review, remote sensing analysis, and process modelling. Geomorphology, 246: 377-393.

George, D. L., Iverson, R. M. (2011) A two-phase debris-flow model that includes coupled evolution of volume fractions, granular dilatancy, and pore-fluid pressure. Italian Journal of Engineering Geology and Environment: 415-424.

He, S., Liu, W., Wang, J. (2015) Dynamic simulation of landslide based on thermo-poro-elastic approach. Computers and Geosciences, 75:24-32.

Huang, Y., Zhang, W., Xu, Q., Xie, P., Hao, L. (2012) Run-out analysis of flow-like landslides triggered by the Ms 8.0 2008 Wenchuan earthquake using smoothed particle hydrodynamics. Landslides, 9(2), 275-283

Huang, H., Yang, K., Lai, S. (2007) Impact force of debris flow on filter dam. Momentum, 9, 2.

Hunter, G., Fell, R. (2003) Travel distance angle for" rapid" landslides in constructed and natural soil slopes. Canadian Geotechnical Journal, 40(6): 1123-1141.

Iverson, R. M., George, D. L. (2015) Modelling landslide liquefaction, mobility bifurcation and the dynamics of the 2014 Oso disaster. Géotechnique: 1-13.

Iverson, R. M., George, D. L., Allstadt, K., Reid, M. E., Collins, B. D., Vallance, J. W., Schilling,S.P., Godt, J.W., Cannon, C.M., Magirl, C.S., Baum, R.L., Coe, J.A., Schulz, W.H., Bower，J.B. (2015) Landslide mobility and hazards: implications of the 2014 Oso disaster. Earth and Planetary Science Letters, 412: 197-208.

Iverson, R. M., Ouyang, C. (2015) Entrainment of bed material by Earth‐surface mass flows: Review and reformulation of depth‐integrated theory. Reviews of Geophysics, 53(1): 27-58.

Jafari N.H., Stark T.D., Merry S. (2013) The July 10 2000 Payatas landfill slope failure. International Journal of Geoengineering Case Histories, 2(3):208-28.

Kirschbaum, D., Stanley, T., Zhou, Y. (2015) Spatial and temporal analysis of a global landslide catalog. Geomorphology, 249: 4-15.

Legros, F. (2002) The mobility of long-runout landslides. Engineering Geology, 63(3): 301-331.

Lavigne, F., Wassmer, P., Gomez, C., Davies, T. A., Sri, D., Iskandarsyah, T., Gaillard, J. C., Fort, M., Texier, P.,Boun, M.,Pratomo, I. (2014) The 21 February 2005, catastrophic waste avalanche at Leuwigajah dumpsite, Bandung, Indonesia. Geoenvironmental

Disasters 1:1-12.

Liang, D., Falconer,R., Lin,B. (2006) Comparison between TVD-MacCormackand ADI-type solvers of the shallow water equations. Advances in Water Resources 29:1833–1845.

Liang, Q. (2010). Flood simulation using a well-balanced shallow flow model.Journal of hydraulic engineering, 136(9), 669-675.

Liu, G., Liu, M. (2003) Smoothed particle hydrodynamics: a meshfree particle method. World Scientific.

Lo, C. M., Lee, C. F., Chou, H. T., Lin, M. L. (2014) Landslide at Su-Hua highway 115.9 k triggered by typhoon Megi in Taiwan. Landslides, 11(2), 293-304.

McDougall S, Hungr O. (2004) A model for the analysis of rapid landslide motion across three-dimensional terrain. Canadian Geotechnical Journal, 41(6): 1084-1097.

Ouyang, C, He S, Xu, Q, Luo, Y., Zhang, W. (2013) A MacCormack-TVD finite difference method to simulate the mass flow in mountainous terrain with variable computational domain. Computers and Geosciences, 52: 1-10.

Ouyang, C., He, S., Tang, C. (2015a) Numerical analysis of dynamics of debris flow over erodible beds in Wenchuan earthquake-induced area. Engineering Geology, 194: 62-72.

Ouyang, C., He, S., Xu, Q. (2015b) MacCormack-TVD finite difference solution for dam break hydraulics over erodible sediment beds. Journal of Hydraulic Engineering, 141(5).

Pastor, M., Haddad, B., Sorbino, G., Cuomo, S., Drempetic, V. (2009) A depth‐integrated, coupled SPH model for flow‐like landslides and related phenomena. International Journal for numerical and analytical methods in geomechanics, 33(2), 143-172.

Pirulli, M. (2005) Numerical modelling of landslide runout. A continuum mechanics approach . Doctoral Dissertation, Politecnico di Torino.

Quecedo, M., Pastor, M., Herreros, M. I., Fernández Merodo, J. A. (2004) Numerical modelling of the propagation of fast landslides using the finite element method. International Journal for Numerical Methods in Engineering,59(6), 755-794.

Savage, S. B., and Hutter, K. (1989) The motion of a finite mass of granular material down a rough incline, Journal of Fluid Mechanics, 199, 177–215.

Tang, C., Hu, J., Lin, M., Angelier, J., Lua, C., Chan, Y., Chu, H. (2009) The Tsaoling landslide triggered by the Chi-Chi earthquake, Taiwan: Insights from a discrete element simulation. Engineering Geology, 106(1-2): 1-19.

Van Leer B. (1979) Towards the ultimate conservative difference scheme. V. A second-order sequel to Godunov's method. Journal of computational Physics, 32(1): 101-136.

Van Westen, C. J., Van Asch, T. W., Soeters, R. (2006) Landslide hazard and risk zonation—why is it still so difficult? Bulletin of Engineering geology and the Environment, 65(2), 167-184.

Wang, G., Sassa, K. (2003) Pore-pressure generation and movement of rainfall-induced landslides: effects of grain size and fine-particle content. Engineering geology, 69(1), 109-125.

Wang, F., Sassa, K. (2010). Landslide simulation by a geotechnical model combined with a model for apparent friction change. Physics and Chemistry of the Earth, Parts A/B/C35,149–161.

Wang, J., Ling, H., Smyth, A. (2008) Failures associated with the 2004 Mindulle Typhoon in Taiwan. Geotechnical and Geological Engineering, 26(1): 79-90.

Xu, Q., Peng D., Li, W., Dong, X., Tang, M., Hu, W., Tang, M., Liu, F. (2016) The 20 December 2015, catastrophic construction waste landslide at Hongao dumpsite, Guangming New District, Shenzhen,China, Natural Hazards and Earth System Sciences Discussion, doi:10.5194/nhess-2016-196.

Yin, Y., Wang, F., Sun, P. (2009) Landslide hazards triggered by the 2008 Wenchuan earthquake, Sichuan, China. Landslides, 6(2), 139-152.

Yin,Y., Li, B., Wang,W., Zhan,L., Xue, Q., Gao,Y., Zhang, N., Chen, H., Liu, T., Li, A. (2016) Mechanism of the December 2015 Catastrophic Landslide at the Shenzhen Landfill and Controlling Geotechnical Risks of Urbanization. Engineering, 2(2): 230 -249.

Zhao, D., Nezami, E., Hashash, Y., Ghaboussi, J. (2006) Three-dimensional discrete element simulation for granular materials. Engineering Computations, 23(7): 749-770.

Zhang Y., Qi M., Ma H. (2006) Slope instability and its control in Shenzhen City. Chinese Journal of Rock Mechanics and Engineering, S2 (in Chinese)

Figures Caption

Fig. 1 Photos of the pre- and post-landslide in Guangming new district. (a) Pleiades satellite image on Dec 18, 2015; (b) Aerial photo of the landslide on Dec 23, 2015.

Fig. 2 The engineering geological map of the landslide.

Fig. 3 The geological and topographical cross section along profile line A-A.

Fig. 4 Particle size distribution of four different samples.

Fig. 5 Monthly rainfall and cumulative rainfall from January 2013 to December 2015 in nearby Tangjia rainfall station.

Fig. 6 Fully liquefied soil in sliding surface.

Fig. 7 Snapshots of computed flow height contours of Guangming landslide at at (a) t=0 s, (b) t=25 s, (c) t=50 s, (d) t=100 s, (e) t=150 s, (f) t=200 s.

Fig. 8 Comparison of numerical results and field investigation results along (a) the main sliding profile A-A, (b) transverse profile B-B and (c) transverse profile C-C.

Fig. 9 Snapshots of the computed flow velocity contours of Guangming landslide at (a) t=25 s, (b) t=50 s, (c) t=100 s, (d) t=150 s, (e) t=200 s.

Fig. 10 Velocity histories over time in four different locations S1-S4 of the main profile.

Fig. 11 The final flow depth contours of Guangming landslide at (a) =0, (b) λ=0.3, (c) λ=0.6, (d) λ=0.85 .

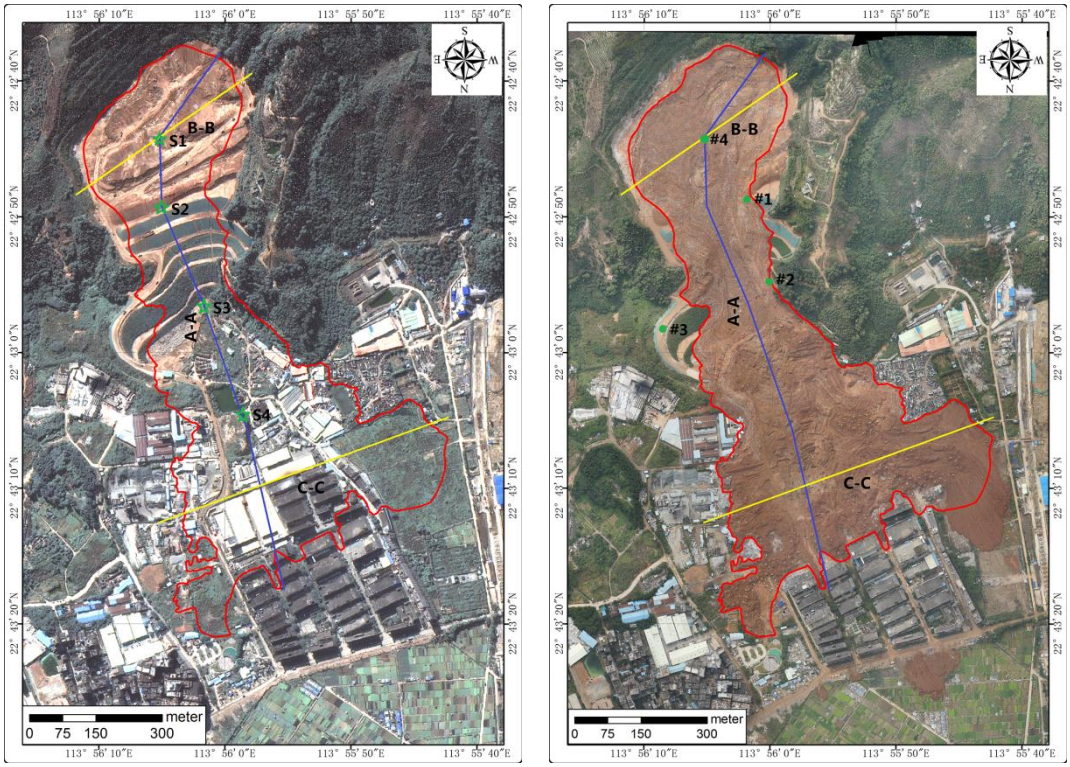

(a) (b)

Fig. 1 Photos of the pre- and post-landslide in Guangming new district. (a) Pleiades satellite image on Dec 18, 2015; (b) Aerial photo 96 of the flowslide on Dec 23, 2015.

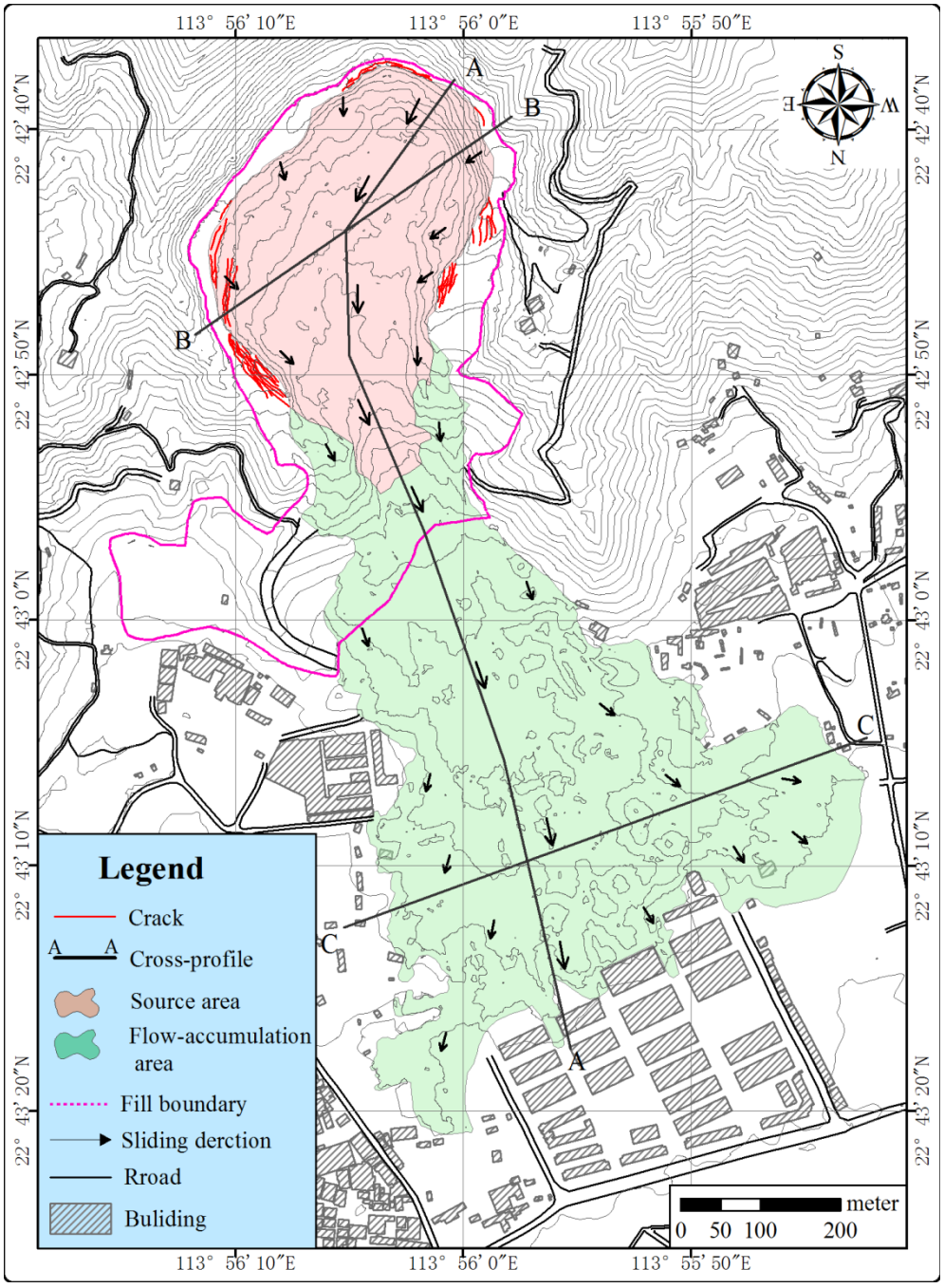

Fig. 2 The engineering geological map of the landslide.

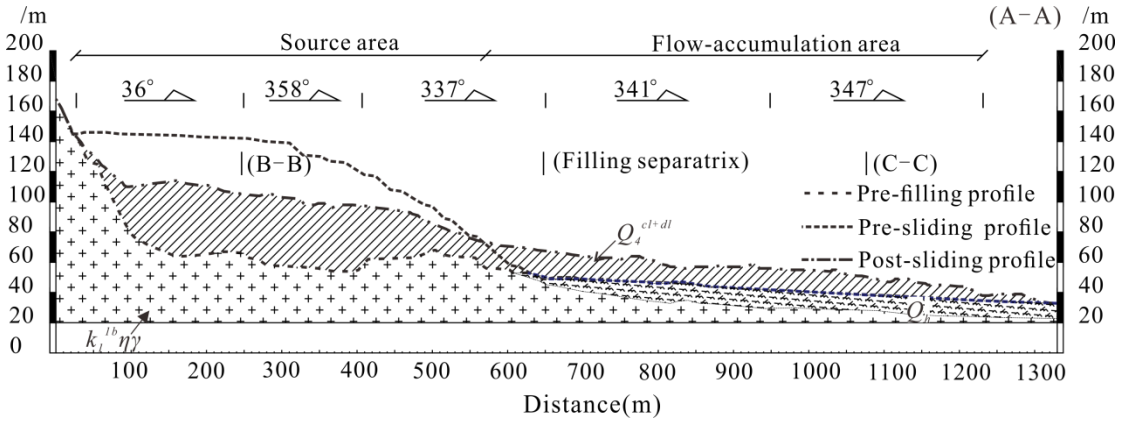

Fig. 3 The geological and topographical cross section along profile line A-A.

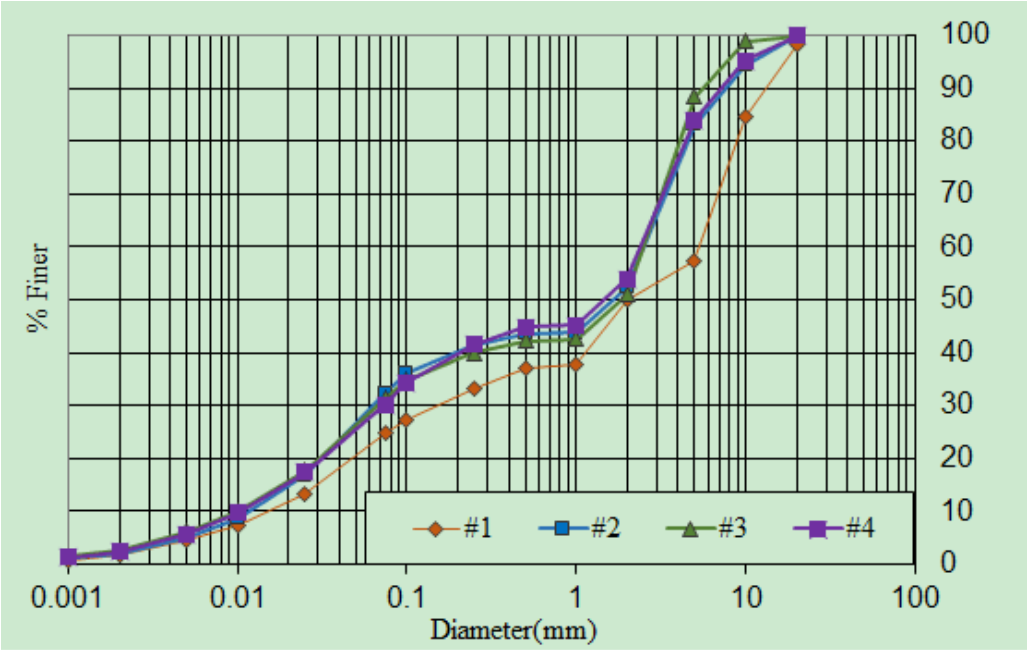

Fig. 4 Particle size distribution of four different samples.

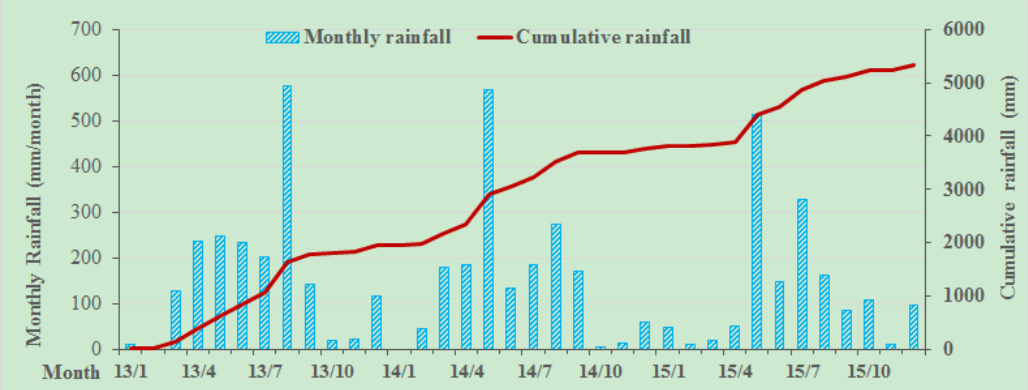

Fig. 5 Monthly rainfall and cumulative rainfall from January 2013 to December 2015 in nearby Tangjia rainfall station.

Fig. 6 Fully liquefied soil in sliding surface.

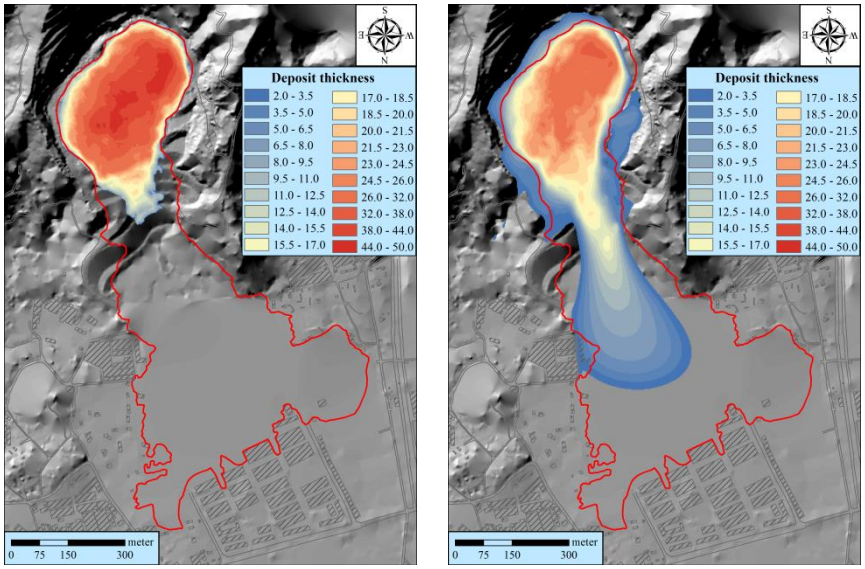

(a) (b)

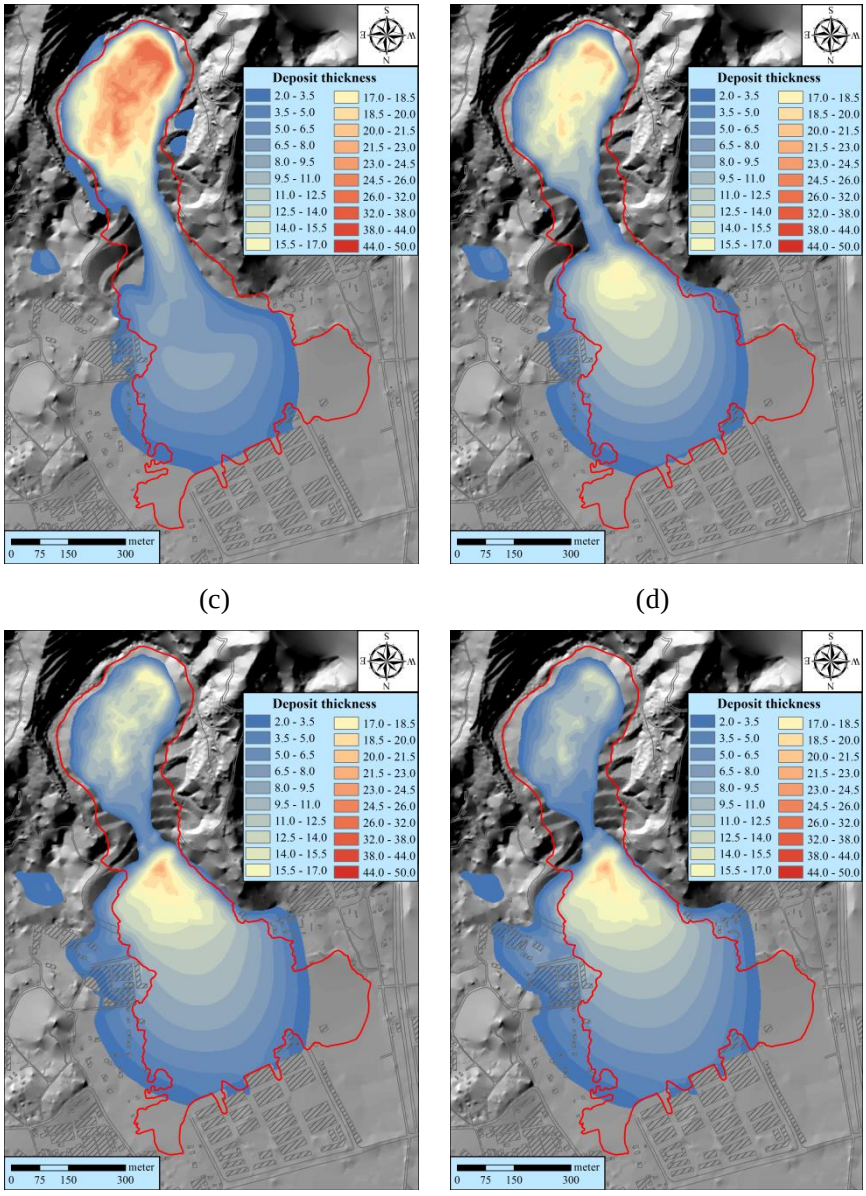

Fig. 7 Snapshots of computed flow height contours of Guangming landslide at at (a) t=0 s, (b) t=25 s, (c) t=50 s, (d) t=100 s, (e) t=150 s, (f) t=200 s.

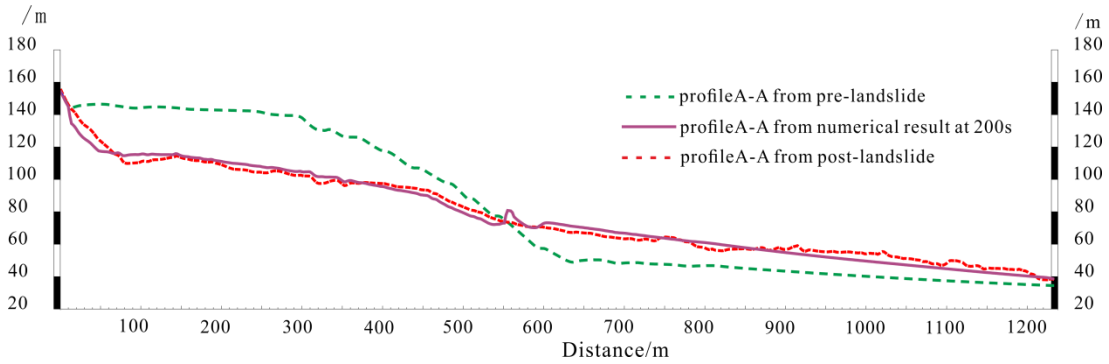

(a)

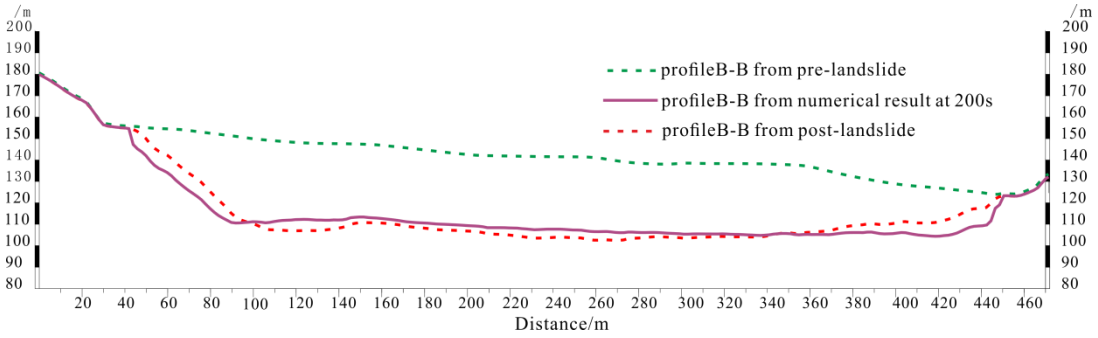

(b)

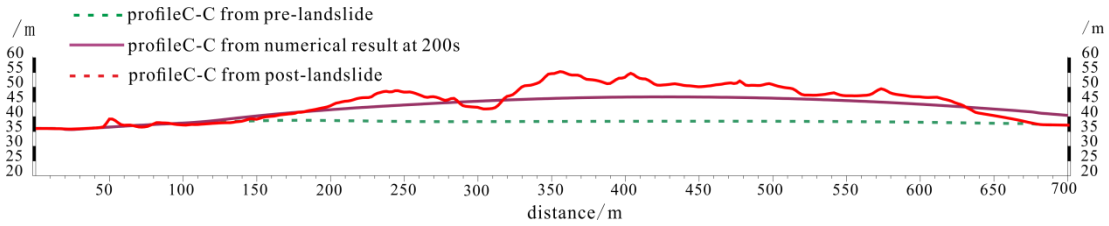

(c)

Fig. 8 Comparison of numerical results and field investigation results along (a) the main sliding profile A-A, (b) transverse profile B-B and (c) transverse profile C-C.

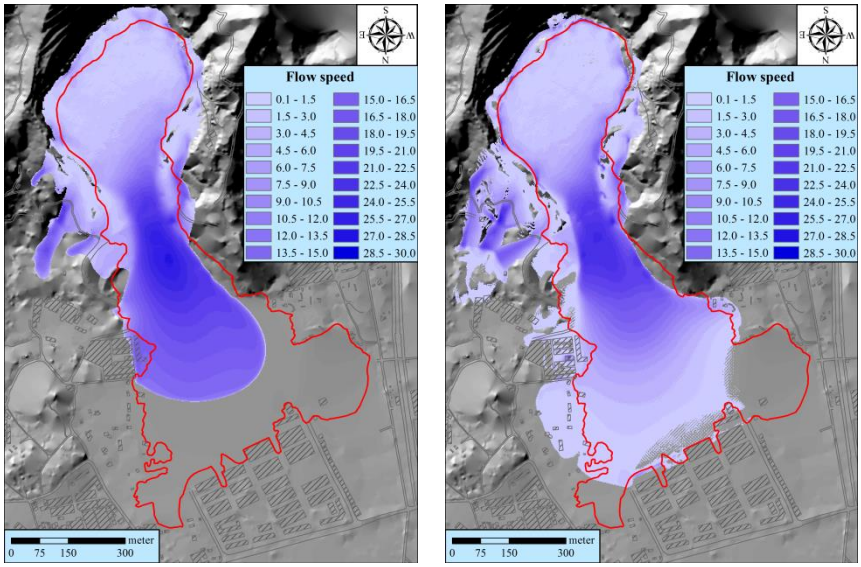

(a) (b)

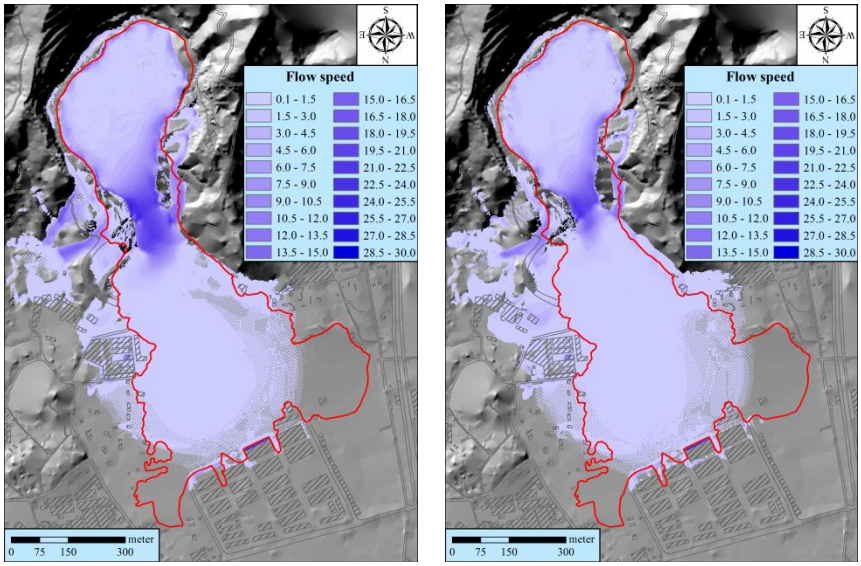

(c) (d)

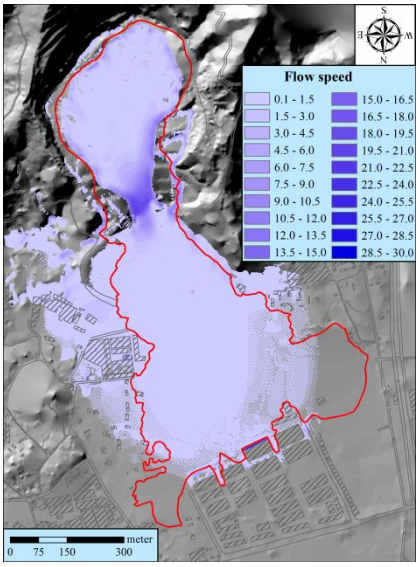

(e)

Fig. 9 Snapshots of the computed flow velocity contours of Guangming landslide at (a) t=25 s, (b) t=50 s, (c) t=100 s, (d) t=150 s, (e) t=200 s.

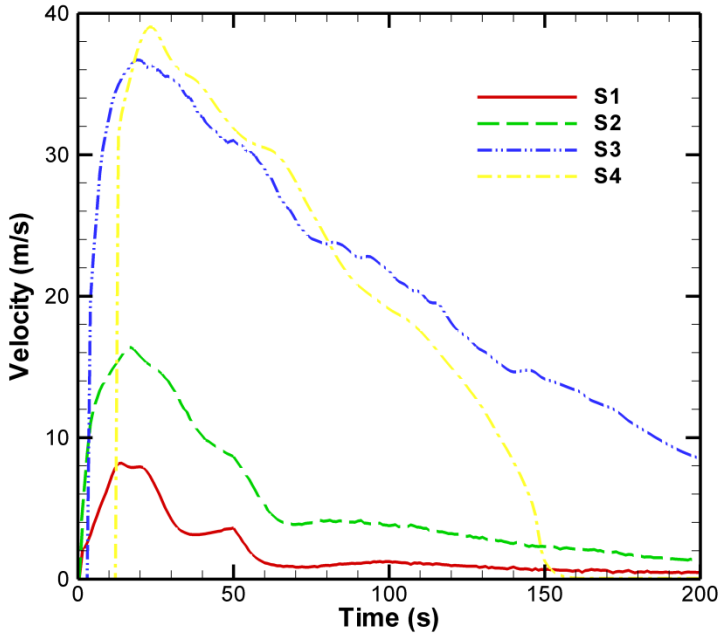

Fig. 10 Velocity histories over time in four different locations S1-S4 of the main profile.

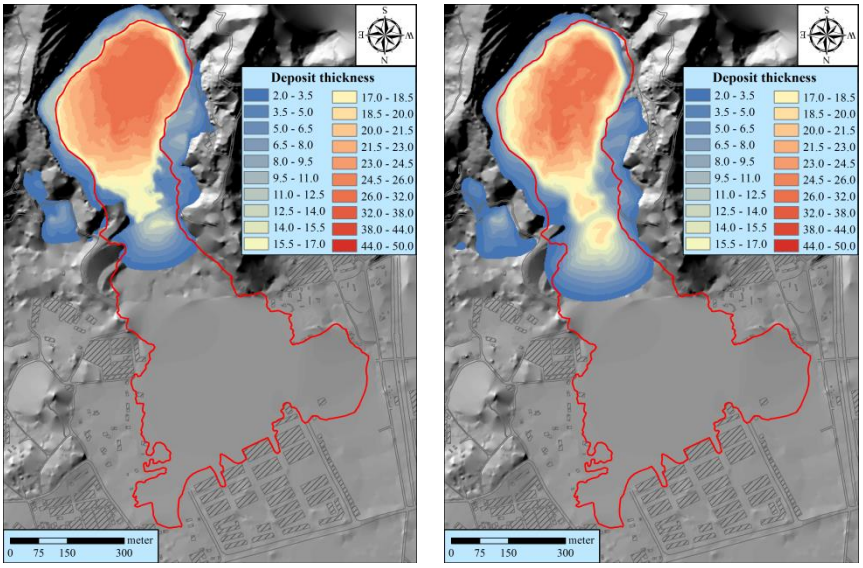

(a) (b)

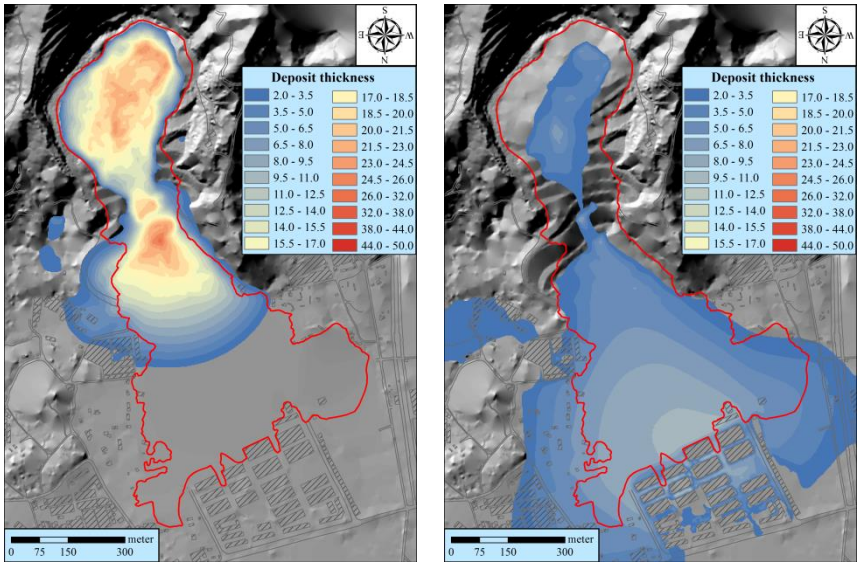

(c) (d)

Fig. 11 The final flow depth contours of Guangming landslide at (a) λ =0, (b) λ =0.3, (c) λ =0.6, (d) λ =0.85 .

Table 1. The mineral composition of waste fill and bedrock by X-ray powder diffraction.

Samples	Mont-morillonite	Glimmerton	Kaolinite	Chlorite	Quartz	K-feldspar	Plagioclase	Calcspar	Dolomite	Sodium amphibole
#1	-	16	-	55	22	4	-	4	-	-
#2	-	20	-	59	19	2	-	-	-	-
#3	-	15	-	59	19	3	-	4	-	-
#4	-	13	-	53	29	5	-	-	-	-
bedrock	-	23	-	20	20	19	18	-	-	-

Click here to access/download

Supplementary Material - for Audio/Video File

Animation of landslide dynamic process.avi